Fuel 366 (2024) 131414

Contents lists available at ScienceDirect

Fuel

journal homepage: www.elsevier.com/locate/fuel

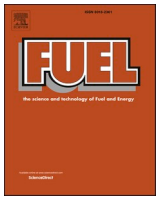

Full Length Article

Using X-ray computed tomography and pore-scale numerical modeling to study the role of heterogeneous rock surface wettability on hydrogen-brine two-phase flow in underground hydrogen storage

Qingqi Zhao [a], Ruichang Guo [a], Nilesh Kumar Jha [b], Mohammad Sarmadivaleh [c], Maxim Lebedev [b], Ahmed Al-Yaseri [d], James McClure [e], Cheng Chen [a,*]

[a] Department of Civil, Environmental and Ocean Engineering, Stevens Institute of Technology, Hoboken, NJ, USA
[b] Centre for Sustainable Energy and Resources, School of Engineering, Edith Cowan University, Australia
[c] Western Australian School of Mines, Mineral, Energy and Chemical Engineering, Curtin University, Australia
[d] Centre for Integrative Petroleum Research, College of Petroleum Engineering and Geosciences, King Fahd University of Petroleum & Minerals, Saudi Arabia
[e] National Security Institute, Virginia Tech, Blacksburg, VA, USA

ARTICLE INFO

Keywords:
Underground hydrogen storage
CT measurement of contact angle
Lattice Boltzmann
Relative permeability
Capillary pressure

ABSTRACT

Underground hydrogen storage (UHS) is receiving increasing attention to address the challenges in hydrogen storage. A crucial aspect of UHS is understanding the transport of hydrogen in subsurface porous media. In this work, hydrogen core flooding experiments were conducted in a sandstone sample and then the pore-scale distribution of hydrogen and brine was visualized using high-resolution X-ray micro-computed tomography (micro-CT). After CT image processing, we measured the surface contact angles (CAs) on rock surfaces and found that the measured CAs followed a log-normal distribution. To investigate the influence of rock surface wettability on the transport properties in the hydrogen-brine-sandstone system, the lattice Boltzmann (LB) method was used to simulate two-phase flows with different surface CA distributions; hydrogen-brine relative permeability and capillary pressure curves through the primary drainage, imbibition, and secondary drainage processes were obtained by LB simulations. X-ray CT scanning showed that hydrogen resided in both large pores and small pores and pore throats after the primary drainage process (i.e., hydrogen displacing brine), whereas after the imbibition process (i.e., brine displacing hydrogen) hydrogen stayed primarily in large pores where the capillary pressure barriers were low. The LB two-phase flow modeling illustrated that water's relative permeability increased whereas hydrogen's relative permeability decreased when the core flooding moved from primary drainage to imbibition; in contrast, when the core flooding moved from imbibition to secondary drainage, water's relative permeability decreased whereas hydrogen's relative permeability increased. Decreasing the surface CA increased the capillary pressure and reduced the hydrogen residual rate, which indicates high hydrogen retrievability and thus is favorable for UHS practice. The change in CA's standard deviation did not cause noticeable changes in water's relative permeability curves, whereas it resulted in noticeable changes in hydrogen's relative permeability curves. This work is the first study that utilizes X-ray micro-CT scanning and pore-scale multiphase flow modeling to quantitatively and comprehensively investigate hydrogen-brine two-phase flow properties under different rock surface wettability distributions. The research findings from this study will advance the understanding of hydrogen transport in an underground storage system and provide essential data for large-scale field studies in UHS.

1. Introduction

The increasing concerns on global warming have led to a search for clean energy alternatives to replace fossil fuels. Hydrogen energy presents a viable solution due to its non-polluting and greenhouse gas-free properties. Hydrogen possesses a high specific energy capacity of 120–142 kJ/g, making it an excellent energy carrier [41]. It can be utilized to store electricity during low demand periods and transformed

* Corresponding author.
E-mail address: cchen6@stevens.edu (C. Chen).

https://doi.org/10.1016/j.fuel.2024.131414
Received 26 July 2023; Received in revised form 7 January 2024; Accepted 4 March 2024
Available online 7 March 2024

into electric energy during peak consumption times [14,24]. Additionally, hydrogen can be used directly in various applications, such as hydrogen vehicles and steel production.

According to the International Energy Agency [20], the global demand for hydrogen is projected to reach 528 million metric tons by 2050 in order to achieve economy-wide net-zero carbon emissions. One significant challenge in achieving this goal is the issue of large-scale hydrogen storage. Surface storage methods, such as high-pressure gas cylinders, hydrogen storage tanks, and adsorption materials, are subject to limitations in terms of long-term, large-volume hydrogen storage, which require further technological advancements [17,42].

An alternative solution to this challenge is underground hydrogen storage (UHS), which offers several advantages over surface storage methods. Firstly, UHS offers a higher storage capacity compared to surface storage methods [34]. Secondly, storing hydrogen underground utilizes subsurface space, thereby saving ground space and reducing costs. Additionally, UHS can benefit from the experiences and established infrastructure of underground gas storage (UGS). There are 667 UGS facilities in operation worldwide, accounting for 424 billion cubic meters of gas storage capacity as of 2022 [25]. These facilities, including wells and pipelines, can potentially be adapted for UHS storage.

Deep saline aquifers and depleted natural gas reservoirs are two types of potential UHS sites. Saline aquifers are permeable subsurface porous media saturated with brine and covered by impermeable cap rocks. Prior to injecting hydrogen, several preparatory steps, such as drilling wells and conducting well tests, must be carried out. In comparison, utilizing depleted natural gas reservoirs as UHS sites can result in a substantial reduction in the initial investment because these reservoirs have produced hydrocarbons for an extended period of time and possess well-established production facilities and extensive data on reservoir structures and rock properties [41]. Given the porous nature of both saline aquifers and depleted gas reservoirs, it is crucial to examine the flow properties in the hydrogen-brine two-phase flow, for example, the relative permeability and capillary pressure within the formation rock.

The relative permeability and capillary pressure are influenced by various factors, including the rock surface wettability, pore structure, interfacial tension, and saturation history. Recent studies have also indicated that the spatial correlation length of rock surface wettability has an influence on the relative permeability curves [12]. Among these factors, rock surface wettability is considered the most important because it regulates the ultimate UHS capacity, containment security, and multi-phase flow patterns, as confirmed by extensive research in the literature [1,2,13]. Therefore, it is imperative to investigate the impact of rock surface wettability on the relative permeability and capillary pressure curves in hydrogen-brine-rock systems. Rock surface wettability, the extent of the phase adsorption on the solid surface, is evaluated through the surface contact angle (CA) [4]. Generally, a surface CA less than 90° implies a water-wet condition, where the water phase adheres to the rock surface and fills small pores, thereby pushing the gas phase to large pores. Conversely, non-water-wet conditions are indicated by a surface CA greater than 90°.

In recent years, the rock surface CAs in the hydrogen-water–rock system have gained increasing attention and been studied using various methods. Yekta et al. [38] determined the rock surface CAs in hydrogen-brine-rock systems by conducting capillary pressure experiments and applying semi-empirical formulations. They simulated temperature and pressure conditions at two different underground depths, with 20 °C and 55 bar for the shallow depth and 45 °C and 100 bar for the deep depth. Their findings showed a receding surface CA of 21.57° for the shallow depth and 34.92° for the deep depth.

Iglauer et al. [21] measured the brine advancing and receding surface CAs on sandstone surfaces in hydrogen atmospheres with varying temperatures, pressures, and stearic acid concentrations. The results showed that surface CAs increased with increasing stearic acid concentrations, pressures, and temperatures. Under the reservoir condition of 50 °C and 10 MPa, the measured brine advancing and receding surface CAs on the pure quartz surface were 20.6° and 16.7°, respectively. Similarly, Ali et al. [2] studied the impact of organic acid types and concentrations on surface CAs. The study revealed a shift in wetting conditions from strong water-wet to intermediate-wet with increasing organic acid concentrations and longer alkyl chains. The advancing surface CAs changed from 40.8° to 91.3° and the receding surface CAs changed from 35.1° to 82.7°, as the rock surface transformed from pristine quartz substrate to an aged surface treated with organic acids with longer alkyl chains (i.e. 10^{-2} M lignoceric acid) at 25 MPa and 323 K. Hashemi et al. [16] utilized the captive-bubble method to measure hydrogen-brine-rock surface CAs and found that the surface CAs ranged from 25° to 45° in underground storage conditions. However, unlike Ali et al. [2] and Iglauer et al. [21], they did not find any relationship between hydrogen-brine-sandstone surface CAs and temperatures, pressures, and salinity.

Jha et al. [22] conducted hydrogen injections in a sandstone rock and then used high-resolution X-ray micro-computed tomography (micro-CT) scanning to study hydrogen-brine distribution at the pore scale. The CT images indicated that a significant amount of hydrogen may be trapped underground after production. To date, only one study (Higgs et al., 2021) has measured the in-situ surface CAs in the hydrogen-brine-sandstone system, resulting in a mean CA value of 39.77°.

The relative permeability and capillary pressure curves in the hydrogen-brine-rock system are typically obtained through core flooding experiments. Due to the novelty of UHS in porous media, there is limited experimental data on the hydrogen-brine-rock system. Yekta et al. [38] measured hydrogen-brine relative permeability and capillary pressure curves based on the classic steady-state technology under varying pressure and temperature conditions (20 °C and 55 bar, and 45 °C and 100 bar). They observed that these conditions had a subtle impact on the relative permeability and capillary pressure curves. Rezaei et al. [32] studied relative permeability of the hydrogen-brine-rock system in the unsteady state. They compared hydrogen-brine relative permeabilities in different back-pressures, temperatures, and rock types, and found that the pore structure had a significant influence on the relative permeability whereas the salinity had a less prominent effect.

An important consideration for relative permeability is the hysteresis, which can significantly influence pore-scale drainage and imbibition, as well as reservoir-scale injections and withdrawal [18,26,30,40]. Delving into this aspect, research conducted by Lysyy et al. [27], utilizing advanced microfluidic techniques, has shed light on the significant impact of relative permeability's hysteresis on pore-scale hydrogen flow. Their findings indicated a pronounced effect of relative permeability's hysteresis on gas trapping, evident by changes in hydrogen relative permeability during imbibition processes. At the reservoir scale, the implications of relative permeability's hysteresis become even more crucial. Bo et al. [5] demonstrated that this relative permeability hysteresis not only persisted but was also amplified during large-scale reservoir operations. Their studies suggested that overlooking the relative permeability hysteresis effect could lead to significant deviations in the calculated relative permeability of hydrogen. Such discrepancies can result in substantial underestimation of the hydrogen storage capacity, thereby directly impacting the effectiveness and reliability of hydrogen storage strategies [35]. Moreover, the relative permeability hysteresis can contribute to phenomena such as bottom water invasion and increased hydrogen trapping [10]. These combined effects can lead to a reduction in the hydrogen yield and may require a reevaluation of storage and retrieval strategies in hydrogen storage reservoirs.

Numerical simulation is a powerful alternative to experimental methods for measuring transport properties, such as relative permeability and capillary pressure. In a recent study by Hashemi et al. [15], the transport properties of the hydrogen-brine two-phase flow were analyzed using a pore network model (PNM). They utilized a

homogeneous surface CA value, obtained from Yekta et al. [38]. The results showed that both rock surface wettability and pore structure significantly influenced the properties of the hydrogen-brine two-phase flow. However, the PNM simplifies many properties of porous media by converting it into spheres connected by cylinders, which can improve the computing efficiency but reduce the computing accuracy. With advancements in the X-ray micro-CT technology, direct pore-scale simulation using the lattice Boltzmann (LB) method can be performed to simulate single- and multi-phase flows in the pore space of the rock. This method is a robust solution to handling complex boundary conditions and pore geometries in multi-phase flow problems, which can be accelerated using graphics processing unit-enhanced parallel computing [6,12,11]. In recent studies, LB multiphase flow simulation has been applied on large, three-dimensional (3D) domains, such as 800 × 800 × 600 lattice unit (lu)^3, to analyze the water-CO_2 two-phase flow [12].

This work investigates hydrogen-brine relative permeability and capillary pressure curves using 3D CT images, obtained from hydrogen-brine core flooding experiments, and LB two-phase flow simulations. The study is organized as follows: First, the raw CT images were segmented into the phases of brine, hydrogen, and sandstone. Next, rock surface CA distribution was measured, which was then utilized to generate auto-correlated Gaussian random fields that represented heterogeneous distribution of rock surface wettability. Particularly, sensitivity analyses were conducted to study the role of different CA distributions having varied mean values and standard deviations on the system's relative permeability and capillary pressure curves. This work analyzed the influences of the rock surface wettability and its heterogeneity on hydrogen transport properties in porous media. The insights give crucial guidance for evaluating future UHS site potentials.

2. Materials and methods

2.1. Core flooding experiments and X-ray micro-CT scanning

The core flooding experiment based on hydrogen injection and withdrawal in a sandstone sample was carried out in the laboratory, with details given in a previous study [22]. The experimental setup was the same as in the previous study [23], as illustrated in Fig. 1. Two groups of X-ray micro-CT images were obtained by scanning the core sample during the primary drainage (PD) and imbibition (IM) stages, separately. Particularly, a Gosford sandstone core plug with a diameter of 5 mm and length of 15 mm was used in the core flooding experiment. The core was initially saturated with 2 molarity NaCl brine and then subjected to one cycle of PD (i.e., hydrogen injection) and one cycle of IM (i.e., brine injection). During the PD stage, the hydrogen flow rate was 0.01 ml/min, leading to a capillary number of 2.49 × 10^{-10}, which was in the range of the capillary numbers encountered in field-scale storage projects [37]. The total injected hydrogen volume was five pore volumes. During the IM stage, brine was injected under a flowrate of 0.01 ml/min, leading to a capillary number of 2.49 × 10^{-10}. The total injected brine volume was five pore volumes. Micro-CT scanning was conducted at the end of each flooding cycle. Particularly, the Xradia Versa XRM CT scanner was used to scan 994 vertical two-dimensional (2D) images, each of which had a spatial resolution of 2 μm per pixel length and dimensions of 984 × 1012 pixels. These 2D images were then reconstructed to obtain the 3D image.

2.2. LB method for pore-scale simulation of multiphase flow in porous media

The color-gradient LB multiphase flow model was used in this study for numerical simulation of immiscible two-phase flow displacement in the sandstone, which was then used to calculate the capillary pressure (i.e., P_c-S_w) curves and relative permeability of the system. The LB method has proven an efficient tool to simulating multiphase flows in complex 3D porous media [12,29], and the LB model used in this study has been extensively tested and published in our previous studies [8,9,12]. Particularly, our LB multiphase flow model has been validated by the comparison between CT-scanned and LB-simulated pore-scale fluid distributions during immiscible two-fluid displacement [8] and the comparison between theoretically-predicted and LB-simulated water saturation evolutions during immiscible two-fluid displacement [28].

In our LB model, the momentum equation is simulated using the D3Q19 lattice structure, which means there are 19 velocity directions in the 3D space. The discrete velocity vectors in D3Q19 are:

$$\begin{cases} (0,0,0) & \text{for} q=0 \\ (\pm 1,0,0) & \text{for} q=1,2 \\ (0,\pm 1,0) & \text{for} q=3,4 \\ (0,0\pm 1,) & \text{for} q=5,6 \\ (\pm 1,\pm 1,0) & \text{for} q=7,8,9,10 \\ (\pm 1,0,\pm 1) & \text{for} q=11,12,13,14 \\ (0,\pm 1,\pm 1) & \text{for} q=15,16,17,18 \end{cases} \quad (1)$$

In order to reduce the computing costs, the mass transfer equation was simulated using a D3Q7 lattice structure [29]. The corresponding velocity vectors in D3Q7 are the first seven vectors in Equation (1). The mass distributions for the wetting fluid and non-wetting fluid are constructed using their densities, ρ^w and ρ^n, and the velocity, **u**:

$$\begin{aligned} g_q^w &= w_q\left[\rho^w\left(1+\mathbf{e}_q\cdot\mathbf{u}\right)+\beta\left(\mathbf{e}_q\cdot\mathbf{n}\right)\rho^n\rho^w/(\rho^n+\rho^w)\right] \quad q=0,1,2,\cdots,6 \\ g_q^w &= w_q\left[\rho^n\left(1+\mathbf{e}_q\cdot\mathbf{u}\right)-\beta\left(\mathbf{e}_q\cdot\mathbf{n}\right)\rho^n\rho^w/(\rho^n+\rho^w)\right] \quad q=0,1,2,\cdots,6 \end{aligned} \quad (2)$$

where weights w_q are 1/3 for $q = 0$ and 1/9 for $q = 1,2,\cdots,6$, and n is the unit vector normal to the fluid–fluid interface. The superscripts *w* and *n* refer to the wetting fluid and nonwetting fluid, respectively. In this study, we used water and brine for wetting fluid interchangeably.

The fluid densities are then calculated as:

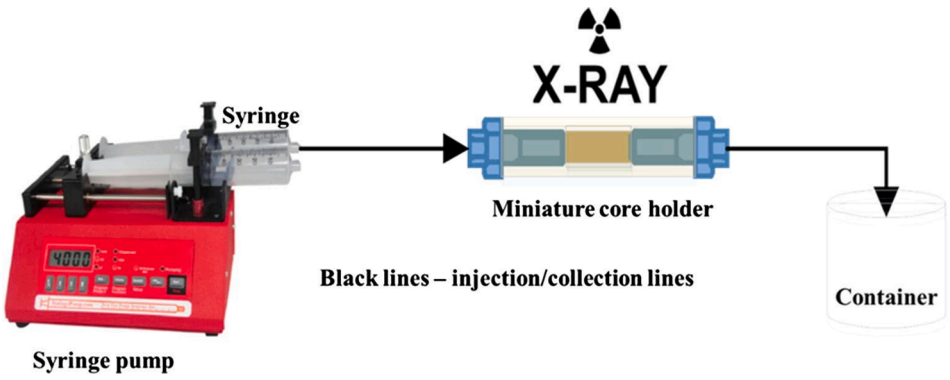

Fig. 1. Experimental setup for hydrogen core flooding experiments and X-ray micro-CT scanning (figure from [23]).

$$\rho^i(\mathbf{x}, t+\Delta t) = \sum_{q=0}^{6} g_q^i(\mathbf{x} - \mathbf{e}_q \Delta t, t) \quad i = w, n \tag{3}$$

In the multi-relaxation-time approach, the collision process is simulated in the moment space. The transformation between moments, m, and the distribution function, f, are written as:

$$\mathbf{m} = M \cdot \mathbf{f}, \mathbf{f} = M^{-1} \cdot \mathbf{m} \tag{4}$$

where M is the transformation matrix, and M^{-1} is the inverse of M.

The particle distribution evolution equation is written as:

$$f_q(\mathbf{x} + \mathrm{e}_q \Delta t, t + \Delta t) - f_q(\mathbf{x}, t) = \sum_{i=0}^{Q-1} M_{qi}^{-1} \Lambda_i (m_i^{eq} - m_i) \quad q = 0, 1, 2, \cdots, 18 \tag{5}$$

where $f_q(\mathbf{x}, t)$ is the particle distribution function at location $\mathbf{x}$ and time t travelling in the q^{th} direction; $f_q(\mathbf{x} + \mathrm{e}_q \Delta t, t + \Delta t)$ is the particle distribution function at the adjacent lattice node after each streaming step in the q^{th} direction; Λ_i is the i^{th} relaxation rate of moment m_i toward its corresponding equilibrium value, m_i^{eq}.

To simulate the interfacial tension, additional terms are incorporated into the non-zero equilibrium moments:

$$\begin{aligned}
m_1^{eq} &= \left(j_x^2 + j_y^2 + j_z^2\right) + \alpha|\mathbf{C}| \\
m_9^{eq} &= \left(2j_x^2 - j_y^2 - j_z^2\right) + \alpha\frac{|\mathbf{C}|}{2}\left(2n_x^2 - n_y^2 - n_z^2\right) \\
m_{11}^{eq} &= \left(j_y^2 - j_z^2\right) + \alpha\frac{|\mathbf{C}|}{2}\left(n_y^2 - n_z^2\right) \\
m_{13}^{eq} &= j_x j_y + \alpha\frac{|\mathbf{C}|}{2} n_x n_y \\
m_{14}^{eq} &= j_y j_z + \alpha\frac{|\mathbf{C}|}{2} n_y n_z \\
m_{15}^{eq} &= j_x j_z + \alpha\frac{|\mathbf{C}|}{2} n_x n_z
\end{aligned} \tag{6}$$

where $j_i j_y$, and j_z are fluid momentums in the x, y, and z directions, respectively; α is the parameter to adjust the interfacial tension; $\mathbf{C}$ is the color gradient; n_x, n_y, and n_z are the components of the unit norm vector, $\boldsymbol{n}$, in the x, y, and z directions, respectively.

In the LB simulation of immiscible two-fluid displacement, a buffer layer with a thickness of six lus was placed at both ends of the rock in the main flow direction. The buffer layer at the inlet was set as H_2 whereas the buffer layer at the outlet was set as water. The pressure boundary condition was applied at the inlet and outlet, and the no-slip boundary condition was applied at rock surfaces. In this work, the coefficient, α, in Equation (6) was set as 0.005. We matched the Ca between the LB model system and the real system to recover the correct ratio of viscous force to interfacial force. Because the Ca number was low, which indicates that the flow velocity is slow and the interfacial tension dominates over the viscous force, the impact of density ratio was negligible. Therefore, in this study the density ratio between H_2 and water was set as one. The rock was initially saturated with water. We gradually changed the pressure difference between the two ends of the rock sample to let the system go through the PD, IM, and secondary drainage (SD) stages. The capillary pressure (i.e., pressure difference between the non-wetting fluid and wetting fluid) and water saturation in the sample were recorded when the flow reached a steady state at each pressure difference. At each water saturation, H_2 and water distribution in the 3D pore space was extracted and then used as the initial condition to simulate the steady-state relative permeability curves. In the simulation of relative permeability, fluid flow was driven by applying a constant external body force with a periodic boundary condition in the main flow direction, which aimed to maintain a constant water saturation in the domain and to mimic fractional flow experiments typically used to measure relative permeability in the laboratory [8]. To address the high demand of computing costs associated with the LB method, a hybrid, multicore central processing unit (CPU)/GPU parallel computing acceleration algorithm was employed in the implementation of the LB model in this study [29,6].

2.3. Generation of auto-correlated CA distribution

Rock surface wettability determines the fluid distribution at the pore scale and is represented by the surface CA. The X-ray CT image dataset obtained at the end of the drainage stage, described in Section 2.1, showed that the surface CA's mean value was 38.9° and standard deviation was 38.5°. Details of rock surface CA measurements based on X-ray CT imaging are given in Section 3. In this study, we used these values as the reference to generate heterogeneous surface CA distributions as described in Table 1. Simulations 1 and 2 are two sensitivity analyses, where the surface CA properties were modified from the reference state. Particularly, Simulation 1 aimed to investigate the influence of the CA's mean value, whereas Simulation 2 aimed to study the role of the CA's standard deviation.

The wettability of a rock surface can be characterized using the static CA measured on the sandstone surface. In our previous study [12], we conducted in-situ measurements of static CAs on the rock surfaces in a Bentheimer sandstone based on high-resolution X-ray micro-CT scanning [36]. The measurements showed that the surface CA distribution follows a lognormal distribution and can be modeled as a Gaussian random field with a spatial correlation length. The log wettability field, $\mathbf{Y}$, is defined as $\mathbf{Y} = \log(\theta)$, where θ is the CA random field. The mean and variance of θ are related to the mean and variance of $\mathbf{Y}$ by $\mu_\theta = e^{\mu_Y + \frac{\sigma_Y^2}{2}}$ and $\sigma_\theta^2 = \left(e^{\sigma_Y^2} - 1\right) \cdot e^{2\mu_Y + \sigma_Y^2}$, respectively [43]. The correlation function of the log wettability field between points x and y in the 3D space, $c_Y(x,y)$, is calculated as $c_Y(x,y) = \sigma_Y^2 exp\left[-\left(\frac{|x_1 - y_1|}{L_1} + \frac{|x_2 - y_2|}{L_2} + \frac{|x_3 - y_3|}{L_3}\right)\right]$, where L_1, L_2, and L_3 are the correlation lengths in the three principal directions [12].

We used the Karhunen-Loève expansion (KLE) method to efficiently generate the heterogeneous wettability field on rock surfaces, which reduces the time and computer memories required compared to other methods that directly generate 3D random fields [39]. In the KLE method, the correlation function of the log wettability field, $c_Y(x,y)$, is decomposed in the form of eigenvalues and eigenfunctions:

$$c_Y(\mathbf{x}, \mathbf{y}) = \sum_{n=1}^{\infty} \lambda_n \psi_n(\mathbf{x}) \psi_n(\mathbf{y}) \tag{7}$$

where λ_n and $\psi_n(\mathbf{x})$ are the n^{th} eigenvalue and eigenfunction, respectively.

The wettability fields are then generated using the KLE method:

$$\mathbf{Y}(\mathbf{x}) = \langle \mathbf{Y}(\mathbf{x}) \rangle + \sum_{n=1}^{\infty} \xi_n \sqrt{\lambda_n} \psi_n(\mathbf{x}) \tag{8}$$

where ξ_n are independent zero-mean Gaussian random variables having a unit variance. In practice, finite terms in the KLE method are employed to approximate the desired random fields [7]. The details of this method

Table 1
Combinations of the mean value and standard deviation of the surface CA for sensitivity analyses. The CA's spatial correlation length is 27.03 pixels, equal to 54.06 μm.

	CA's mean value	CA's standard deviation
Reference value	38.9°	38.5°
Simulation 1	20.0°	38.5°
	60.0°	38.5°
Simulation 2	38.9°	20.0°

were given in [12,39]. In the next step, the surface wettability of the sandstone is constructed by mapping the generated wettability field onto the surface of the Bentheimer sandstone.

3. Results and discussion

3.1. Surface CA distribution

The fluid distributions of the hydrogen and brine in porous media are affected by many factors, including the rock types, rock surface wettability, and capillary number [11]. Fig. 2a and 2b illustrate the 2D cross sections of the gray-scale 3D CT reconstructions after the PD and IM stages, respectively and Fig. 2c and 2D illustrate the profiles of the hydrogen and brine saturations at the pore scale, which were based on CT image segmentation using the package of Trainable Weka Segmentation [3]. Fig. 2c illustrates that hydrogen occupied both large and small pores after the PD stage. The presence of hydrogen in small pores and pore throats enhanced hydrogen phase connectivity and thus was favorable for hydrogen mobility. Fig. 2d shows that after the IM process, hydrogen was displaced by brine and pushed into the large pores due to the low capillary energy barrier there. This process caused reduction in hydrogen phase connectivity and thus led to decreased hydrogen mobility. Particularly, a significant portion of hydrogen remained within large pores, resulting in a 41 % residual saturation after the IM process. Considering that the hydrogen saturation after the PD stage was 65 % [22], it was suggested that a considerable amount of hydrogen cannot be displaced by brine during the IM process, indicating a relatively low hydrogen retrievability. Therefore, a sandstone formation has the potential to store hydrogen for an extended period, and the stored hydrogen can be extracted by injecting a cushion gas with high rock surface wettability, such as nitrogen [22].

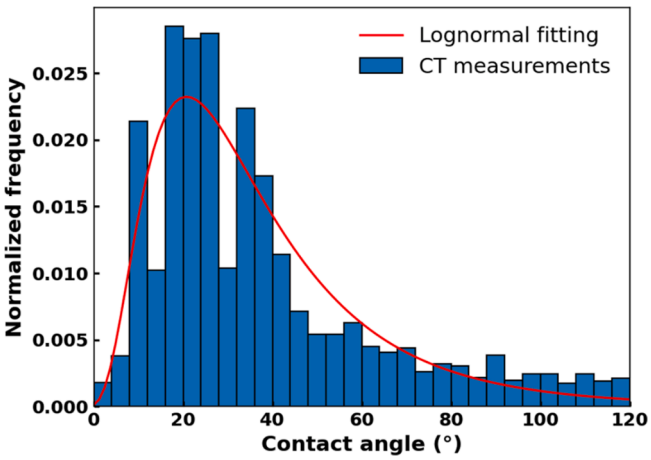

Fig. 3. Surface CA distributions measured from 3D X-ray micro-CT scanning.

Fig. 3 shows the distribution of the measured rock surface CAs based on the segmented CT images using a CA measurement algorithm [19]. This method utilized a two-stage algorithm for determining contact angles in porous media. The first stage is an initial coarse estimation, which uses a uniform mesh to categorize pixels and identify contact points at phase interfaces. Average normal vectors at these contact points provide initial angle estimates. The process is then refined in the second stage by fitting lines (in 2D) or planes (in 3D) to these contact

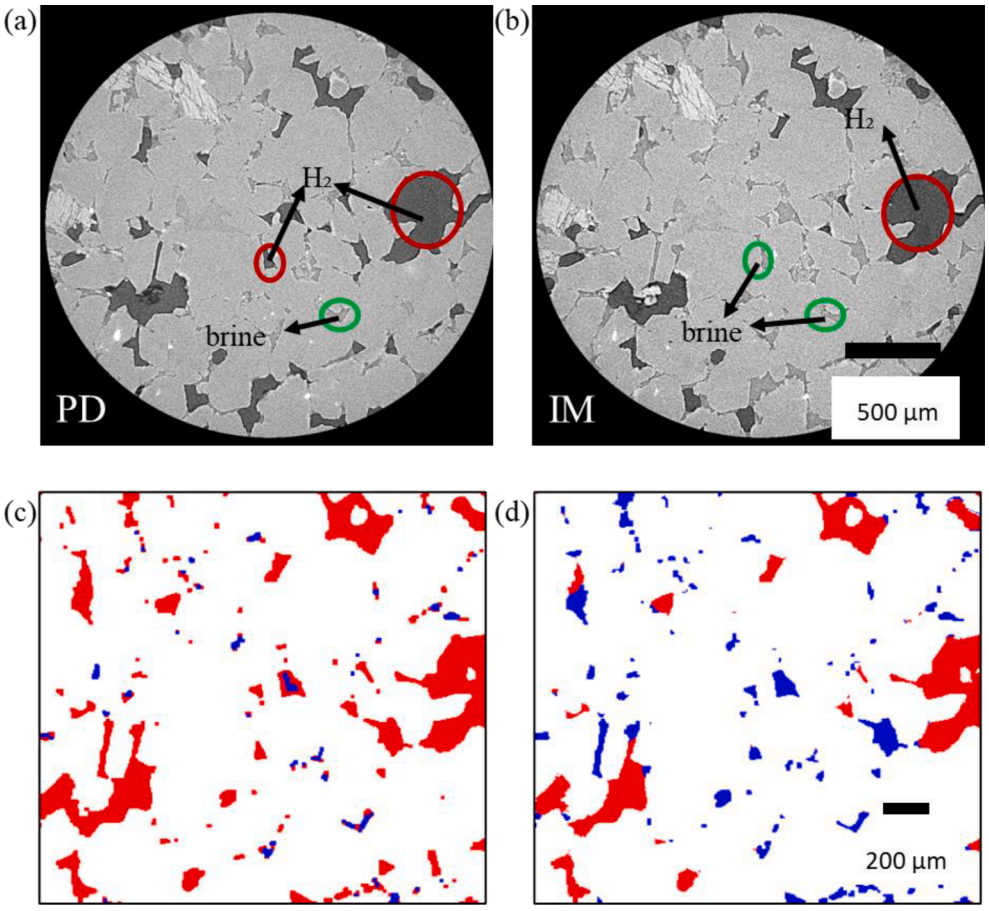

Fig. 2. 2D cross sections of gray-scale X-ray micro-CT images showing the saturation profiles of hydrogen and brine after (a) PD, and (b) IM processes, and the segmented 2D cross sections of the micro-CT images showing the saturation profiles of hydrogen (red) and brine (blue) after (c) PD, and (d) IM processes.

points, with the final contact angle precisely calculated from these adjusted normal vectors. A total of 10,015 surface CAs were measured after the PD process. The measured surface CAs had a mean value of 38.9°, a median value of 19.0°, and a standard deviation of 38.5°. The CA's mean value indicated that the rock surface was strongly water-wet, which meant that the affinity between rock surface and brine was higher than that between rock surface and hydrogen. This is consistent with the observation of the pore-scale fluid distributions after the PD and IM processes as demonstrated in Fig. 2, which indicated that brine was the wetting fluid whereas hydrogen was the non-wetting fluid. The high heterogeneity of the surface CA distribution, as evidenced by the wide range of measured values and large standard deviation, was further demonstrated by the fact that the mean was larger than the median and a long tail was observed at the right side of the distribution. Some surface CAs were larger than 90°, suggesting local rock surfaces that were hydrogen wet. The skewed distribution of the measured CAs was fitted using a log-normal model [12].

The segmented 3D X-ray image dataset of the sandstone was imported into the LB model as solid boundaries for numerical simulation of two-phase flow in the pore space. Particularly, the computational domain had dimensions of 300 × 300 × 300 voxels, with a spatial resolution of 2 μm per pixel length. Fig. 4 illustrates the 2D cross sections of the pore-scale distributions of hydrogen and brine obtained from X-ray CT scanning LB multi-phase flow modeling. These pore-scale fluid configurations were obtained after five pore volumes of hydrogen injection during the PD stage. The hydrogen saturations were 65.0 % and 67.3 % in the CT image and LB-simulated result, respectively. The LB modeling result showed good agreement with the CT image. Both CT imaging and LB modeling results indicate that brine preferentially occupied small pores and throats, whereas hydrogen resided in both small and large pores. It was easy for hydrogen to stay in large pores because it was the non-wetting fluid and large pores had relatively low capillary energy barriers. The presence of hydrogen in small pores was caused by the drainage process, in which a capillary pressure was imposed on the rock sample to drive hydrogen to flow into the pore space and to displace brine, leading to connected channels of hydrogen throughout the pore throats.

3.2. Effect of CA's mean value

The mean value of the rock surface CAs, as measured from micro-CT imaging, was found as 38.9° with a standard deviation of 38.5°. To study the influence of the rock surface wettability on hydrogen transport in the storage system, the surface CA's mean value was artificially changed to 20.0° and 60.0° in the LB model and then compared with the reference case that had a CA mean value of 38.9. All of the three cases had the same standard deviation as measured from the CT image (i.e., 38.5°).

Capillary pressure plays a crucial role in determining the phase saturation distribution in porous media, leading to a significant impact on relative permeability curves that regulate the two-phase flow. Capillary trapping, which is caused by the capillary pressure, has been extensively investigated in CO_2 sequestration [33]. In a UHS project, it is desirable to minimize capillary trapping to facilitate the extraction of hydrogen during the withdrawal stage [31]. The LB multiphase flow model simulated the P_c-S_w curves under three different CA's mean values (20.0°, 38.9°, 60.0°).

Fig. 5a illustrates the P_c-S_w curves of the three scenarios having different surface CA's mean values. The P_c-S_w curves shifted from right to left when the rock surface CA's mean value changed from 20.0° to 60.0°, indicating a reduction in the brine amount trapped in the pores after the drainage stage and an increase in the hydrogen amount trapped in the pores after the IM stage. In addition, the P_c-S_w curves showed a shift from the upside to the downside as the mean value of the surface CAs increased, suggesting a decline in the capillary pressure when the rock surface became less water-wet. In a UHS project, a low residual rate of hydrogen is desirable because residual hydrogen (i.e., hydrogen trapped in the storage system) is immobilized and thus cannot be extracted. This observation shows that a strongly water-wet rock surface condition is favorable for UHS due to its lower hydrogen residual rate.

The entry capillary pressures in the PD stage were found to be negative for all the three scenarios. This was because the rock surface CA heterogeneity led to local hydrogen-wet rock surfaces, where the CA values were greater than 90.0°. The entry capillary pressure increased with the decrease of the surface CA's mean value. This was because when the CA's mean value decreased, under the same CA's standard deviation (i.e., 38.5°), the number of the CA values greater than 90.0° decreased, indicating that less rock surfaces were hydrogen wet.

Relative permeability significantly influences multi-phase flows in porous media [31]. The relative permeability curves were simulated under three different surface CA's mean values (20.0°, 38.9°, and 60.0°), as illustrated in Fig. 5b–5d. Water's relative permeability increased whereas hydrogen's relative permeability decreased when the core flooding process changed from PD to IM. This was because during the IM stage, water flowed back into the rock, occupied small pores and pore throats, and displaced hydrogen into large pores, leading to isolated hydrogen blobs and consequently reduced mobility and relative permeability for hydrogen. In contrast, when the core flooding process changed from IM to PD, water's relative permeability decreased whereas

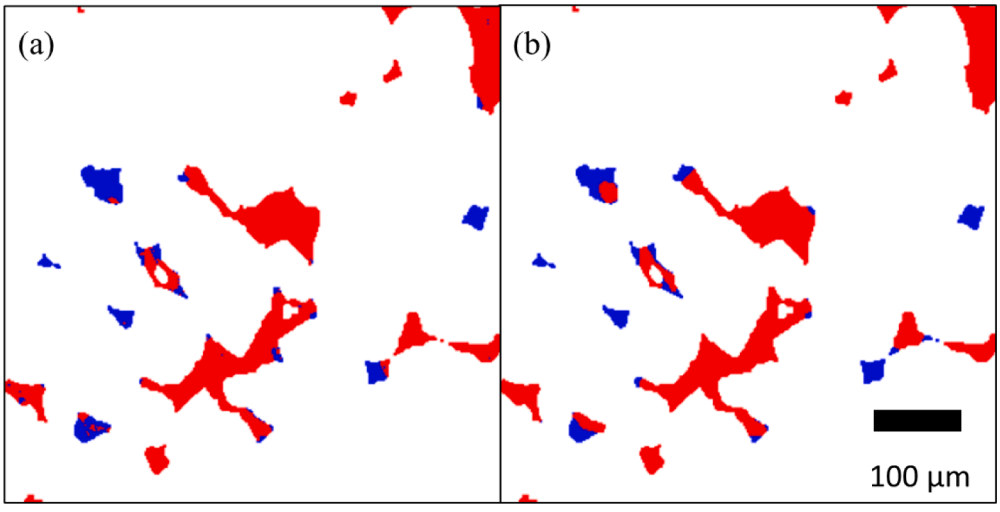

Fig. 4. 2D cross sections of the pore-scale distributions of hydrogen (red) and brine (blue) obtained from (a) X-ray micro-CT scanning, and (b) LB multi-phase flow simulation.

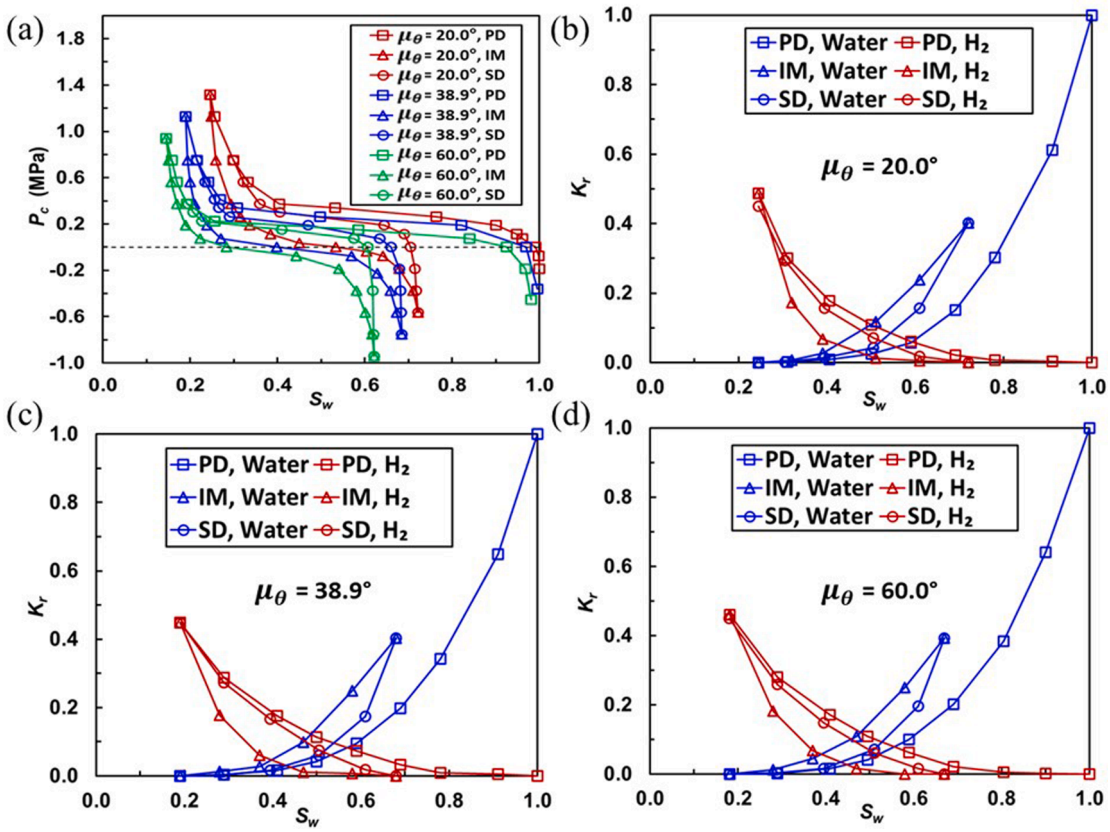

Fig. 5. (a) P_c-S_w curves with different CA's mean values (20.0°, 38.9°, and 60.0°), and relative permeability curves with CA's mean values of (b) 20.0°, (c) 38.9°, and (d) 60.0° in the PD, IM, and SD processes. The surface CA's standard deviation for all the three cases is equal to 38.5° and the CA's spatial correlation length is 27.03 pixels, equal to 54.06 μm.

hydrogen's relative permeability increased. This was because during the PD stage, hydrogen was forced to flow into the rock under the capillary pressure, leading to connected flow channels of hydrogen and consequently reduced mobility and relative permeability for water. This phenomenon was observed for all the three scenarios that had different CA's mean values.

3.3. Effect of CA's standard deviation

The standard deviation of surface CAs represents the rock surface's wettability heterogeneity. With high wettability heterogeneity, the local surface CA can deviate significantly from the CA's mean, which may alter the two-phase flow property at the larger scale. Therefore, it is crucial to study the influence of wettability heterogeneity on UHS. This study investigated two CA's standard deviations: a reference value (38.5°) that was measured from the experiment using X-ray CT, and a reduced value (20.0°) that was artificially changed from the reference value.

Fig. 6a illustrates the LB-simulated P_c-S_w curves for the two scenarios having different CA's standard deviations. The capillary pressure curves for the two scenarios are nearly identical except at the beginning of the PD stage. This finding suggests that the impact of rock surface wettability heterogeneity on the P_c-S_w curve was negligible at the larger scale. In other words, although the surface wettability heterogeneity may change the distribution of hydrogen and brine locally, the capillary force for the entire rock sample did not change noticeably.

Negative entry capillary pressures were observed in both scenarios. The absolute value of the entry capillary pressure for the reference case in which the CA's standard deviation was 38.5° was larger than that of the case with a CA's standard deviation of 20.0°. This was because with a smaller CA's standard deviation (20.0°), less rock surfaces were hydrogen wet, which reduced the absolute value of the negative entry pressure.

Fig. 6b–6d demonstrate the LB-simulated relative permeability curves through the PD, IM, and SD stages. The change in CA's standard deviation did not cause noticeable changes in water's relative permeability curves. Conversely, the change in CA's standard deviation resulted in noticeable changes in hydrogen's relative permeability curves. Particularly, through the PD, IM, and SD stages, it was consistently shown that a smaller CA's standard deviation (20.0°) enhanced the relative permeability of hydrogen compared to the reference case where the CA's standard deviation was 38.5°. This was because in both scenarios the mean CA was 38.9°, indicating an overall water-wet rock surface. Therefore, in both scenarios, water formed a thin coating on rock surfaces and flowed within this 2D, well-connected water layer. As a consequence, the connectivity and effective permeability of water depended primarily on the average CA of the entire rock surface and was relatively insensitive to the local heterogeneity (i.e., standard deviation) in the rock surface CA. Conversely, hydrogen flowed primarily near pore centers because it was the non-wetting fluid. A large standard deviation in the CA (38.5°) may cause a small portion of local CA values larger than 90.0°, leading to local, hydrogen-wet surfaces. If these hydrogen-wet surfaces occur in relatively small pores, hydrogen may be trapped in these small pores, which reduced the overall mobility of hydrogen and consequently decreased the effective permeability of hydrogen.

4. Conclusions and implications

This study utilized X-ray micro-CT scanning and pore-scale numerical simulation to investigate the distribution and transport properties of injected hydrogen in a geological storage system. We specifically investigated the effect of rock surface wettability heterogeneity on the

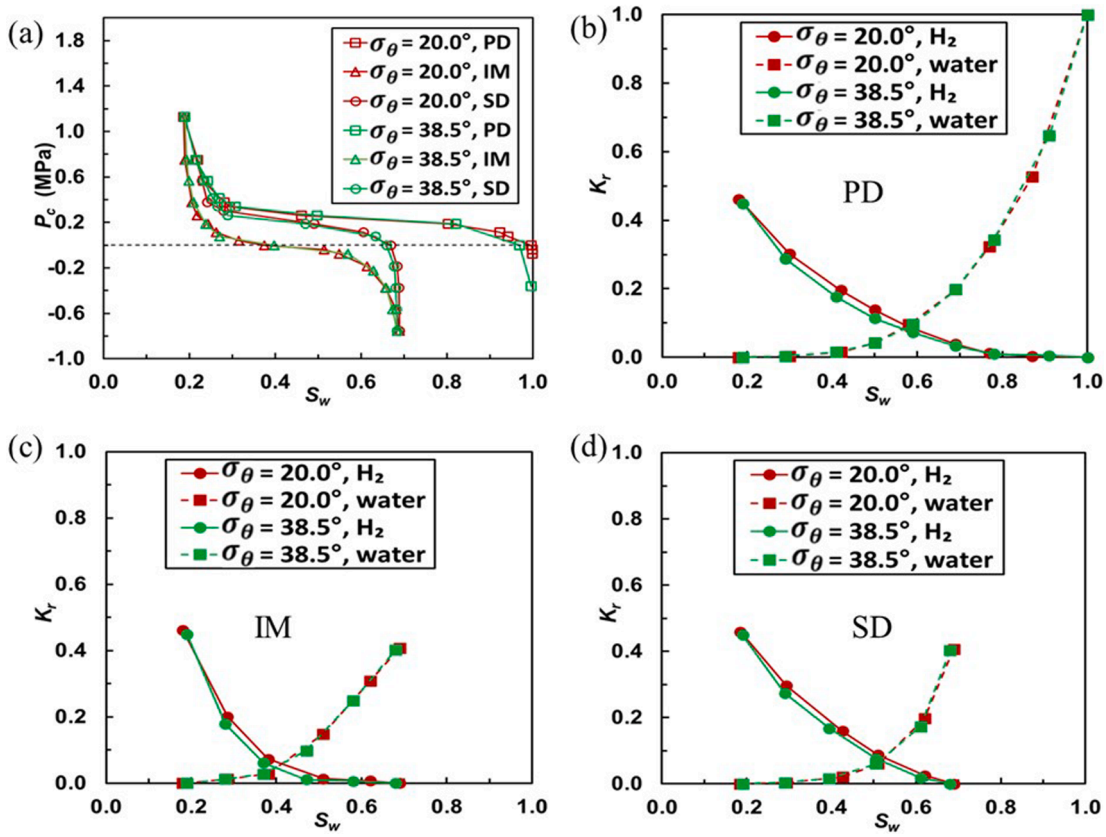

Fig. 6. (a) LB-simulated P_c-S_w curves of different surface CA's standard deviations (20.0° and 38.5°), and LB-simulated relative permeability curves in the (b) PD, (c) IM, and (d) SD processes. The surface CA's mean value is 38.9° in both cases and the CA's spatial correlation length is 27.03 pixels, equal to 54.06 μm.

relative permeability and capillary pressure curves in a hydrogen-brine-sandstone system. The hydrogen core flooding experiments were conducted in one PD-IM cycle and then the surface CA distributions were measured using CT scanning. With the CT measurement as the base case, a sensitivity analysis was conducted by generating various surface CA distributions, which were then input into the LB model for two-phase flow simulations. The LB method simulated the two-phase flows in the sandstone rock sample for a PD-IM-SD cycle. Based on the LB modeling, the relative permeability curves, capillary pressure curves, and fluid distribution at the pore scale were obtained.

The X-ray micro-CT imaging showed that rock surface CAs followed a log-normal distribution; hydrogen resided in both large pores and small pores and pore throats after the PD process, whereas after the IM process hydrogen stayed primarily in large pores where the capillary pressure barriers were low. The LB two-phase flow modeling illustrated that water's relative permeability increased whereas hydrogen's relative permeability decreased when the core flooding moved from PD to IM; in contrast, when the core flooding moved from IM to SD, water's relative permeability decreased whereas hydrogen's relative permeability increased. Decreasing the surface CA increased the capillary pressure and reduced the hydrogen residual rate, which indicates high hydrogen retrievability and thus is favorable for UHS practice. The change in surface CA's standard deviation did not cause noticeable changes in water's relative permeability curves, whereas it resulted in noticeable changes in hydrogen's relative permeability curves.

This work is the first study that utilizes X-ray micro-CT scanning and pore-scale multiphase flow modeling to quantitatively and comprehensively investigate hydrogen-brine two-phase flow properties under different rock surface wettability distributions. The research findings from this study advance the understanding of hydrogen transport in an underground storage system, which has critical implications to the safe and economical operations in UHS projects. Particularly, rock surface wettability changes the mobility of hydrogen in subsurface porous media and thus affects the performance of the UHS. Combining X-ray micro-CT imaging with pore-scale LB multiphase flow modeling provides a powerful tool for studying hydrogen migration and retrievability in a geological storage system. The relative permeability and capillary pressure curves modeled by the LB method can be used as the input in large-scale UHS reservoir simulations.

CRediT authorship contribution statement

Qingqi Zhao: Writing – review & editing, Writing – original draft, Visualization, Validation, Software, Methodology, Investigation, Formal analysis, Data curation, Conceptualization. **Ruichang Guo:** Validation, Software, Methodology, Investigation, Formal analysis, Conceptualization. **Nilesh Kumar Jha:** Visualization, Validation, Methodology, Investigation, Data curation, Conceptualization. **Mohammad Sarmadivaleh:** Validation, Resources, Project administration, Methodology, Conceptualization. **Maxim Lebedev:** Resources, Investigation, Data curation. **Ahmed Al-Yaseri:** Investigation. **James McClure:** Validation, Software, Resources, Methodology, Investigation. **Cheng Chen:** Writing – review & editing, Writing – original draft, Supervision, Resources, Project administration, Methodology, Investigation, Funding acquisition, Formal analysis, Data curation, Conceptualization.

Declaration of competing interest

The authors declare that they have no known competing financial interests or personal relationships that could have appeared to influence the work reported in this paper.

Data availability

Data will be made available on request.

Acknowledgement

The authors would like to thank Stevens Institute of Technology for the financial support of a startup package.

References

[1] Al-Anssari S, Ali M, Alajmi M, Akhondzadeh H, Khaksar Manshad A, Kalantariasl A, et al. Synergistic effect of nanoparticles and polymers on the rheological properties of injection fluids: implications for enhanced oil recovery. Energy Fuel 2021;35(7): 6125–35. https://doi.org/10.1021/acs.energyfuels.1c00105.
[2] Ali M, Jha NK, Al-Yaseri A, Zhang Y, Iglauer S, Sarmadivaleh M. Hydrogen wettability of quartz substrates exposed to organic acids: implications for hydrogen geo-storage in sandstone reservoirs. J Pet Sci Eng 2021;207:109081. https://doi.org/10.1016/j.petrol.2021.109081.
[3] Arganda-Carreras I, Kaynig V, Rueden C, Eliceiri KW, Schindelin J, Cardona A, et al. Trainable Weka Segmentation: a machine learning tool for microscopy pixel classification. Bioinformatics 2017;33(15):2424–6. https://doi.org/10.1093/bioinformatics/btx180.
[4] Arshadi M, Gesho M, Qin T, Goual L, Piri M. Impact of mineralogy and wettability on pore-scale displacement of NAPLs in heterogeneous porous media. J Contam Hydrol 2020;230:103599. https://doi.org/10.1016/j.jconhyd.2020.103599.
[5] Bo Z, Boon M, Hajibeygi H, Hurter S. Impact of experimentally measured relative permeability hysteresis on reservoir-scale performance of underground hydrogen storage (UHS). Int J Hydrogen Energy 2023;48(36):13527–42. https://doi.org/10.1016/j.ijhydene.2022.12.270.
[6] Chen C, Wang Z, Majeti D, Vrvilo N, Warburton T, Sarkar V, et al. Optimization of lattice Boltzmann simulation with graphics-processing-unit parallel computing and the application in reservoir characterization. SPE J 2016;21(04):1425–35. https://doi.org/10.2118/179733-PA.
[7] Chen C, Zeng L, Shi L. Continuum-scale convective mixing in geological CO2 sequestration in anisotropic and heterogeneous saline aquifers. Adv Water Resour 2013;53:175–87. https://doi.org/10.1016/j.advwatres.2012.10.012.
[8] Fan M, Dalton LE, McClure J, Ripepi N, Westman E, Crandall D, et al. Comprehensive study of the interactions between the critical dimensionless numbers associated with multiphase flow in 3D porous media. Fuel 2019;252: 522–33. https://doi.org/10.1016/j.fuel.2019.04.098.
[9] Fan M, McClure JE, Armstrong RT, Shabaninejad M, Dalton LE, Crandall D, et al. Influence of clay wettability alteration on relative permeability. Geophys Res Lett 2020;47(18):e2020GL088545. https://doi.org/10.1029/2020GL088545.
[10] Gao J, Kong D, Peng Y, Zhou Y, Liu Y, Zhu W. Pore-scale mechanisms and hysteresis effect during multi-cycle injection and production process in underground hydrogen storage reservoir. Energy 2023;283:129007. https://doi.org/10.1016/j.energy.2023.129007.
[11] Guo R, Dalton L, Crandall D, McClure J, Wang H, Li Z, et al. Role of heterogeneous surface wettability on dynamic immiscible displacement, capillary pressure, and relative permeability in a CO2-water-rock system. Adv Water Resour 2022;165: 104226. https://doi.org/10.1016/j.advwatres.2022.104226.
[12] Guo R, Dalton LE, Fan M, McClure J, Zeng L, Crandall D, et al. The role of the spatial heterogeneity and correlation length of surface wettability on two-phase flow in a CO2-water-rock system. Adv Water Resour 2020;146:103763. https://doi.org/10.1016/j.advwatres.2020.103763.
[13] Haghighi OM, Zargar G, Khaksar Manshad A, Ali M, Takassi MA, Ali JA, et al. Effect of environment-friendly non-ionic surfactant on interfacial tension reduction and wettability alteration; implications for enhanced oil recovery. Energies 2020; 13(15):15. https://doi.org/10.3390/en13153988.
[14] Hanley ES, Deane JP, Gallachóir BÓ. The role of hydrogen in low carbon energy futures–a review of existing perspectives. Renew Sustain Energy Rev 2018;82(P3): 3027–45.
[15] Hashemi L, Blunt M, Hajibeygi H. Pore-scale modelling and sensitivity analyses of hydrogen-brine multiphase flow in geological porous media. Sci Rep 2021;11(1): 8348. https://doi.org/10.1038/s41598-021-87490-7.
[16] Hashemi L, Glerum W, Farajzadeh R, Hajibeygi H. Contact angle measurement for hydrogen/brine/sandstone system using captive-bubble method relevant for underground hydrogen storage. Adv Water Resour 2021;154:103964. https://doi.org/10.1016/j.advwatres.2021.103964.
[17] Heinemann N, Alcalde J, Miocic JM, Hangx SJT, Kallmeyer J, Ostertag-Henning C, et al. Enabling large-scale hydrogen storage in porous media – the scientific challenges. Energ Environ Sci 2021;14(2):853–64. https://doi.org/10.1039/D0EE03536J.
[18] Higgs S, Wang YD, Sun C, Ennis-King J, Jackson SJ, Armstrong RT, et al. Direct measurement of hydrogen relative permeability hysteresis for underground hydrogen storage. Int J Hydrogen Energy 2024;50:524–41. https://doi.org/10.1016/j.ijhydene.2023.07.270.
[19] Ibekwe A, Pokrajac D, Tanino Y. Automated extraction of in situ contact angles from micro-computed tomography images of porous media. Comput Geosci 2020; 137:104425. https://doi.org/10.1016/j.cageo.2020.104425.
[20] IEA. Global hydrogen review 2021 (CC BY 4.0); 2021. https://www.iea.org/reports/global-hydrogen-review-2021.
[21] Iglauer S, Ali M, Keshavarz A. Hydrogen wettability of sandstone reservoirs: implications for hydrogen geo-storage. Geophys Res Lett 2021;48(3): e2020GL090814. https://doi.org/10.1029/2020GL090814.
[22] Jha NK, Al-Yaseri A, Ghasemi M, Al-Bayati D, Lebedev M, Sarmadivaleh M. Pore scale investigation of hydrogen injection in sandstone via X-ray micro-tomography. Int J Hydrogen Energy 2021;46(70):34822–9. https://doi.org/10.1016/j.ijhydene.2021.08.042.
[23] Jha NK, Lebedev M, Iglauer S, Ali M, Roshan H, Barifcani A, et al. Pore scale investigation of low salinity surfactant nanofluid injection into oil saturated sandstone via X-ray micro-tomography. J Colloid Interface Sci 2020;562:370–80. https://doi.org/10.1016/j.jcis.2019.12.043.
[24] Lazarou S, Vita V, Diamantaki M, Karanikolou-Karra D, Fragoyiannis G, Makridis S, et al. A simulated roadmap of hydrogen technology contribution to climate change mitigation based on representative concentration pathways considerations. Energy Sci Eng 2018;6(3):116–25. https://doi.org/10.1002/ese3.194.
[25] Losson L. Underground gas storage in the world - 2022 status. Cedigaz; 2022, December 7. https://www.cedigaz.org/underground-gas-storage-in-the-world-2022-status/.
[26] Lysyy M, Fernø MA, Ersland G. Effect of relative permeability hysteresis on reservoir simulation of underground hydrogen storage in an offshore aquifer. J Storage Mater 2023;64:107229. https://doi.org/10.1016/j.est.2023.107229.
[27] Lysyy M, Føyen T, Johannesen EB, Fernø M, Ersland G. Hydrogen relative permeability hysteresis in underground storage. Geophys Res Lett 2022;49(17): e2022GL100364. https://doi.org/10.1029/2022GL100364.
[28] McClure JE, Li Z, Sheppard AP, Miller CT. An adaptive volumetric flux boundary condition for lattice Boltzmann methods. Comput Fluids 2020;210:104670. https://doi.org/10.1016/j.compfluid.2020.104670.
[29] McClure JE, Wang H, Prins JF, Miller CT, Feng W-C. Petascale application of a coupled CPU-GPU algorithm for simulation and analysis of multiphase flow solutions in porous medium systems. In: 2014 IEEE 28th international parallel and distributed processing symposium; 2014. p. 583–92. https://doi.org/10.1109/IPDPS.2014.67.
[30] Pan B, Liu K, Ren B, Zhang M, Ju Y, Gu J, et al. Impacts of relative permeability hysteresis, wettability, and injection/withdrawal schemes on underground hydrogen storage in saline aquifers. Fuel 2023;333:126516. https://doi.org/10.1016/j.fuel.2022.126516.
[31] Pan B, Yin X, Ju Y, Iglauer S. Underground hydrogen storage: influencing parameters and future outlook. Adv Colloid Interface Sci 2021;294:102473. https://doi.org/10.1016/j.cis.2021.102473.
[32] Rezaei A, Hassanpouryouzband A, Molnar I, Derikvand Z, Haszeldine RS, Edlmann K. Relative permeability of hydrogen and aqueous brines in sandstones and carbonates at reservoir conditions. Geophys Res Lett 2022;49(12): e2022GL099433. https://doi.org/10.1029/2022GL099433.
[33] Singh K, Jung M, Brinkmann M, Seemann R. Capillary-dominated fluid displacement in porous media. Annu Rev Fluid Mech 2019;51(1):429–49. https://doi.org/10.1146/annurev-fluid-010518-040342.
[34] Wallace RL, Cai Z, Zhang H, Zhang K, Guo C. Utility-scale subsurface hydrogen storage: UK perspectives and technology. Int J Hydrogen Energy 2021;46(49): 25137–59. https://doi.org/10.1016/j.ijhydene.2021.05.034.
[35] Wang H, Xin Y, Kou Z, Qu Y, Wang L, Ning Y, et al. Numerical study of the efficiency of underground hydrogen storage in deep saline aquifers, rock springs uplift, Wyoming. J Clean Prod 2023;421:138484. https://doi.org/10.1016/j.jclepro.2023.138484.
[36] Wang YD, Shabaninejad M, Armstrong RT, Mostaghimi P. Deep neural networks for improving physical accuracy of 2D and 3D multi-mineral segmentation of rock micro-CT images. Appl Soft Comput 2021;104:107185. https://doi.org/10.1016/j.asoc.2021.107185.
[37] Wei N, Gill M, Crandall D, McIntyre D, Wang Y, Bruner K, et al. CO2 flooding properties of Liujiagou sandstone: influence of sub-core scale structure heterogeneity. Greenhouse Gases Sci Technol 2014;4(3):400–18. https://doi.org/10.1002/ghg.1407.
[38] Yekta AE, Manceau J-C, Gaboreau S, Pichavant M, Audigane P. Determination of hydrogen-water relative permeability and capillary pressure in sandstone: application to underground hydrogen injection in sedimentary formations. Transp Porous Media 2018;122(2):333–56. https://doi.org/10.1007/s11242-018-1004-7.
[39] Zhang D, Lu Z. An efficient, high-order perturbation approach for flow in random porous media via Karhunen-Loève and polynomial expansions. J Comput Phys 2004;194(2):773–94. https://doi.org/10.1016/j.jcp.2003.09.015.
[40] Zhang H, Zhang Y, Al Kobaisi M, Iglauer S, Arif M. Effect of cyclic hysteretic multiphase flow on underground hydrogen storage: a numerical investigation. Int J Hydrogen Energy 2024;49:336–50. https://doi.org/10.1016/j.ijhydene.2023.08.169.
[41] Zivar D, Kumar S, Foroozesh J. Underground hydrogen storage: a comprehensive review. Int J Hydrogen Energy 2021;46(45):23436–62. https://doi.org/10.1016/j.ijhydene.2020.08.138.
[42] Züttel A. Hydrogen storage methods. Naturwissenschaften 2004;91(4):157–72. https://doi.org/10.1007/s00114-004-0516-x.
[43] Chen C, Zeng L. Using the level set method to study the effects of heterogeneity and anisotropy on hyporheic exchange. Water Resour Res 2015;51:3617–34. https://doi.org/10.1002/2014WR016444.